PAPER

# Optimal design of optomechanical uncooled infrared focal plane array with integrated metalens

Physica Scripta

PAPER

# Optimal design of optomechanical uncooled infrared focal plane array with integrated metalens

RECEIVED
10 October 2023

REVISED
23 November 2023

ACCEPTED FOR PUBLICATION
4 December 2023

PUBLISHED
14 December 2023

**Zhendong Luo**[1], **Huwang Hou**[2], **Yiyuan Zhang**[1], **Wenlan Li**[1], **Peng Zhang**[1,*] **and Yang Zhao**[1,3,*]

[1] CAS Key Laboratory of Mechanical Behavior and Design of Materials, Department of Precision Machinery & Precision Instrumentation, University of Science and Technology of China, Hefei 230026, People's Republic of China
[2] CAS Key Laboratory of Mechanical Behavior and Design of Materials, Department of Modern Mechanics, University of Science and Technology of China, Hefei 230022, People's Republic of China
[3] Key Laboratory of Precision Scientific Instrumentation of Anhui Higher Education Institutes, University of Science and Technology of China, People's Republic of China
[*] Authors to whom any correspondence should be addressed.

**E-mail:** zhp9036@mail.ustc.edu.cn **and** yangz1@ustc.edu.cn

**Keywords:** uncooled infrared detector, integrated metalens, FPA, Bi-material cantilever

## Abstract

Optomechanical uncooled infrared (IR) detectors based on the thermal deformation of bi-material micro-cantilever have proved of significant potential in the IR imaging fields. However, compared to other uncooled infrared detectors, the optomechanical type relies on the mechanical deformation of the thermomechanical cantilevers, which compete for space with the absorbers and isolation beams, resulting in limited sensitivity. By integrating a designed metalens, large deformation, high thermal isolation, and high effective fill factor can be achieved simultaneously. Several pixel designs of optomechanical uncooled IR focal plane array (FPA) with designed integrated metalens are evaluated and optimized through numerical simulation. High thermal conversion efficiency $H = 0.016$ and thermomechanical sensitivity $S_T = 0.264\ \mu\text{m K}^{-1}$ are simultaneously achieved with an inherent noise-equivalent temperature difference(NETD) value of 3.9 mK at the preset $60\mu\text{m} \times 60\mu\text{m}$ pixels. Using Figure of Merit(FOM) as a comprehensive evaluation of NETD and response time, the optimized structure can be improved by up to 40% over the original structure.

## 1. Introduction

Infrared thermal imaging technology has been widely used in many fields, such as precision guidance and reconnaissance in the military, medical diagnosis [1–4], industrial inspection [5, 6], fire monitoring [7], etc [8–10]. Compared with photon IR detectors, uncooled IR detectors are more widely used in the non-military field for their ability to work at ambient temperature, which brings lower cost and power consumption. Furthermore, among various types of uncooled detectors, the optomechanical detectors based on the thermal response of bi-material micro-cantilever have been researched a lot [11, 12] and shown significant potentials [13–16] for their simple fabricating, cost-reducing, and more importantly, readout integrated circuits(ROIC) removing [10]. So that the parasitic heat from ROIC is eliminated and there is no thermal leakage path caused by the electrical contacts between pixels and substrate. The bi-material cantilever will induce deflection when heated by incident radiation for uneven thermal expansion of the two cantilever materials, as shown in figure 1(a). This deflection makes the visible light in the optical readout path, which will be received by a visible charge-coupled device(CCD), modulated by the movement of the reflector [17, 18]. By measuring the deflection of the cantilever optically, the incident radiation can be obtained. Nevertheless, a pixel unit in optical readout FPA consists of three parts, thermal isolation beams, thermomechanical cantilever, and IR absorption plate (visible light reflecting plate), all of which have an impact on FPA performance respectively. Moreover, the space available in a pixel is limited, causing a competition between the three parts and making it difficult to improve them simultaneously.

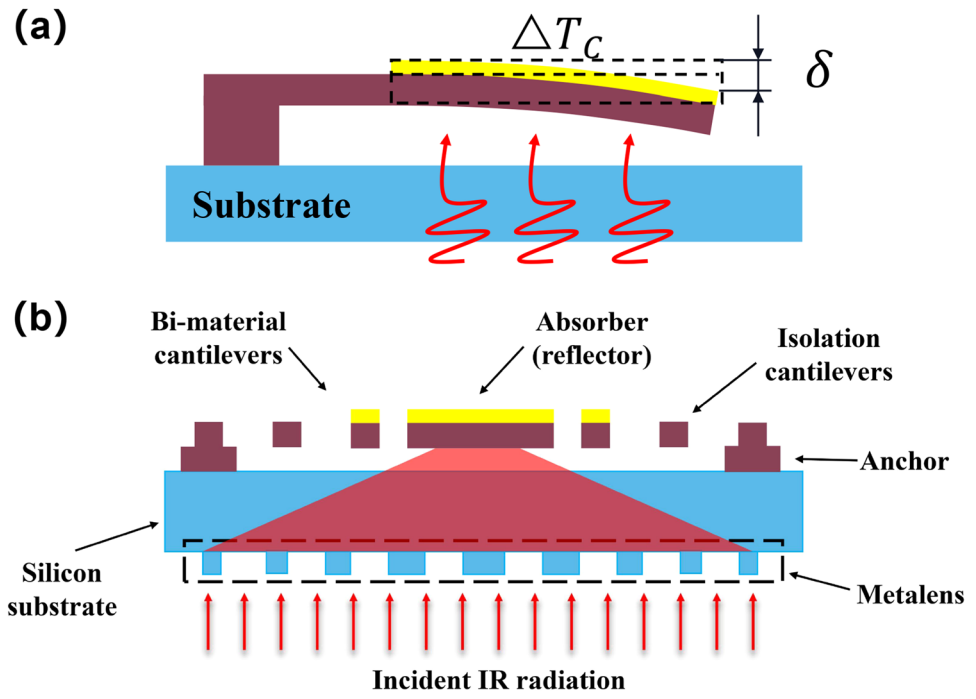


**Figure 1.** (a) Schematic diagram of bi-material microcantilever detection principle. (b) Illustration of the IR detector integrated with the metalens. The metalens is integrated on the back of the substrate and focuses the IR radiation on the absorber at the front side of the substrate correspondingly.

To achieve higher combination performance, some researchers sought solutions from the structure design and optimization. Zhao proposed a two-layer pixel structure design to arrange the three parts in 3D space [19]. Compared with the traditional single-layer ones, this design has more available space for the layout of bi-material thermomechanical cantilevers and thermal isolation beams under a high fill factor, thus the thermal response performance of the system has improved significantly. However, the two-layer designs increase the complexity of fabrication due to the multiple sacrificial layer processes, resulting in low yield and high costs. The group of Q. Zhang developed a substrate-free bi-material FPA with optimized multi-fold interval metallized legs [20–22]. The multi-fold cantilever was designed with long thermomechanical cantilevers in total length and a decent fill factor. However, in order to avoid the mutual cancellation of thermal deformation between adjacent cantilevers, thermomechanical cantilevers, and thermal isolation beams can only be arranged alternately. Despite the long total length of deformation cantilever, the staggered thermal isolation beams block the thermal conduction from the absorber to the outside thermomechanical cantilevers, which leads to the reduction of the total deformation. M. Fatih Toy proposed a nested structure, which consists of an absorber in the pixel center and several isolation beams inserted around the absorber like 'frog legs' [23]. This nested structure allows single thermomechanical cantilevers longer than the pixel size, bringing larger thermomechanical deformation under the same total length. Compared with the structures putting all the components on one pixel, it breaks the limit of the pixel size in one direction and provides more freedom for structure designing. However, when there are long cantilevers, the fill factors of both multi-fold structure and nested structure are usually below 50% [20–23], severely limiting the detector sensitivity. On the other hand, some other researchers enhanced the performance of detectors by finding substitute materials, but always be plagued by manufacturing incompatibilities [24–27].

In our previous effort to improve the performance of FPA, a polarization-insensitive and wide-band metalens has been designed and fabricated for long-wave IR detectors [28]. As shown in figure 1(b), the metalens is integrated on the back of the substrate of the long-wave infrared FPA and focuses the IR radiation on the absorber at the front side of the substrate correspondingly. The monochromatic focusing efficiency of metalens is up to 86%, and the average focusing efficiency in the wide spectral from 8 $\mu$m to 14 $\mu$m reaches 80% [28]. With the designed metalens, it becomes possible to achieve a high effective fill factor with a small IR absorber, leaving more space for the layout of thermomechanical cantilevers and isolation beams. Therefore, it is an effective way to solve the competition between the three factors and thus improve the IR detector performance in all aspects. Hence, this work investigates several optimal designs of optomechanical FPA combined with integrated metalens and the optimized pixel structure is verified both theoretically and numerically.

## 2. Design and optimization

As illustrated in figure 1(a), in bi-material microcantilever based uncooled infrared detector, the signal experienced two conversions: the temperature change $\triangle T_s$ of IR source to the temperature rise $\triangle T_c$ of bi-material cantilevers, and the temperature rise $\triangle T_c$ to the thermal deflection $\delta$ of bi-material cantilevers. Hence, the thermal response can be divided into two parts as:

$$S = \frac{\delta}{\triangle T_s} = \frac{\triangle T_c}{\triangle T_s} \times \frac{\delta}{\triangle T_c} = H^* S_T \tag{1}$$

where $H$ is the thermal conversion efficiency of the focal plane array and $S_T$ is the thermomechanical sensitivity of bi-material cantilevers. For a given incident IR radiation, under the constraints of predetermined element size, it is significant not only to enhance the temperature rise but also to improve the thermomechanical sensitivity in an FPA design [29].

### 2.1. Thermal design of FPA

Considering a pixel in the FPA initially at thermal equilibrium with the surroundings, the temperature rise in the cantilever due to the temperature change of the target IR source can be expressed as:

$$H = \frac{\triangle T_c}{\triangle T_s} = \frac{\alpha A_{ab} \varepsilon \tau_0 \pi (\frac{dP}{dT_t})}{4F_{no}{}^2 (G_{leg} + G_{rad})} \tag{2}$$

where $A_{ab}$ is element absorption area, $\varepsilon$ the absorber emissivity (= 0.8), $F_{no}$ the f/# of IR imaging lens (= 1), $\tau_0$ the transmissivity of the IR system including IR lens and IR window of the vacuum chamber (=0.9), and $\left(\frac{dP}{dT_t}\right) = 0.63W/(m^2Ksr)$ is the fraction of the radiative energy emitted by the source at temperature $T_t$ (~300 K) within the 8–14 $\mu$m spectral band. $\alpha$ is the absorption rate of radiation into the absorbing material, which can denoted by [30]:

$$\alpha = 1 - \exp\ (-4l_p \pi \kappa / \lambda) \tag{3}$$

where $\kappa$ is the absorption coefficient of absorbing material, $\lambda$ the wavelength of IR radiation, and $l_p$ is the absorption length of the infrared radiation in the absorbing material. $G_{leg}$ and $G_{rad}$ are the thermal conductance of the thermal isolation beam and the radiative thermal conductance of pixels, for a single long straight thermal isolation beam which can be expressed as:

$$G_{leg} = \frac{A_{leg} k}{L_{leg}}$$

$$G_{rad} = 4A_{pixel}(\varepsilon_1 + \varepsilon_2)\sigma T^3 \tag{4}$$

where $A_{leg}$ is the cross-sectional area of the isolation beam, $k$ the thermal conductivity of the leg material and $L_{leg}$ the length of the cantilever, $A_{pixel}$ the total pixel area, $\sigma$ the Boltzmann constant, $T$ the pixel temperature (~300 K), $\varepsilon_1$ and $\varepsilon_2$ are the emissivity of the two cantilever materials, respectively.

### 2.2. Thermomechanical design of FPA

The thermomechanical sensitivity $S_T$ of a single cantilever can be expressed as [19]:

$$S_T = \frac{\delta}{\triangle T_C} = 3(\alpha_1 - \alpha_2)\left(\frac{n+1}{K}\right)\left(\frac{L^2_m}{d_2}\right) \tag{5}$$

where $L_m$ is the length of the thermal deformation cantilever, $\alpha_1$ and $\alpha_2$ are the thermal expansion coefficients of cantilever materials respectively, $d_2$ is the thickness of absorbing material film, and $n$ is the ratio of two materials of cantilever thickness. Here, $K$ is a structure parameter, which can be expressed as:

$$K = 4 + 6n + 4n^2 + \Phi n^3 + \frac{1}{\Phi n}$$

$$n = \frac{d_1}{d_2}; \Phi = \frac{E_1}{E_2} \tag{6}$$

where $d_1$ is the thickness of reflective material film, $E$ is the elastic modulus.

### 2.3. FPA layout designs

FPA under the preset pixel size 60 $\mu$m × 60 $\mu$m is designed here with Au and Si $N_x$ as the two materials of bi-material cantilever and Si as substrate. Table 1 lists the physical properties of $SiN_x$ and Au. For given $L_m$ and $d_2$, under the chosen materials, thermomechanical sensitivity $S_T$ varies as $f(n)$, which can be denoted by:

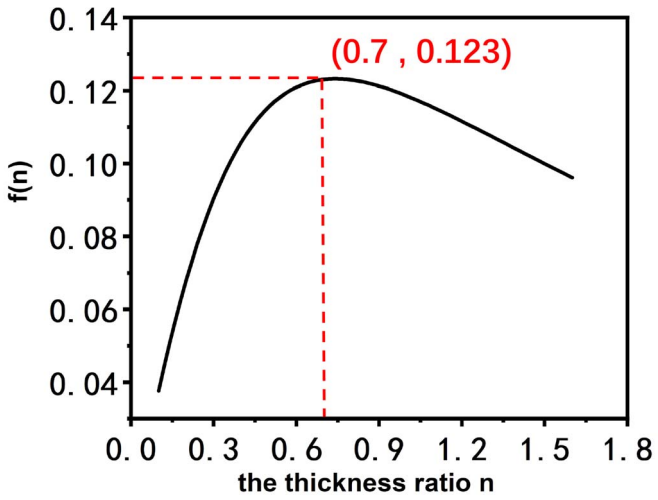


**Figure 2.** $f(n)$ as a function of the thickness ratio $n$ showing the optimum thickness ratio $n \sim 0.7$.

**Table 1.** The physical properties of Si $N_x$ and Au.

| | Density $\rho \times 10^3$ kg/ m$^3$ | Young's modulus $E$ (GN/ m$^2$) | Expansion coefficient $\alpha \times 10^{-6}$K$^{-1}$ | Emissivity $\varepsilon$ | Thermal conductivity $k$ W/(mk) |
|---|---|---|---|---|---|
| Si $N_x$ | 2.4 | 180 | 0.8 | 0.8 | 5.5 |
| Au | 19.30 | 73 | 14.2 | 0.01 | 296 |

$$f(n) = \frac{n+1}{K} = \frac{n+1}{4 + 6n + 4n^2 + \Phi n^3 + \frac{1}{\Phi n}} \tag{7}$$

For $SiN_x$-Au bi-material cantilever, $f(n)$ reaches maximum as $n \sim 0.7$ (figure 2). The thickness of $SiN_x$ film is set as $d_2 = 0.5\ \mu m$. The detailed optimization of the film thickness will be discussed later. With $n = 0.7$, the thickness of Au film is set as $d_{Au} = 0.35\ \mu$m. Moreover, the distance between adjacent legs or absorber is set to be 2 $\mu$m following microfabrication standards for MEMS structure.

It is worth noting that the thermomechanical sensitivity $S_T$ varies as the square of the length of bi-material cantilever in a unidirectional cantilever model in equation (5). Thus, nested structure [23] was adopted, making it possible for FPA element to have single-direction deformation cantilever longer than the pixel size. Pixel structures designed are shown in figure 3(a). Based on the initial nested structure, a two-step optimization procedure is proposed and the optimization effect has been evaluated in both double-stage and triple-stage designs. Group 1 (a, b, c) are the double-stage nested structures with different layouts, while group 2 (a, b, c) are the triple-stage ones. In each group, design (a) is the initial nested design, and design (b) is the optimized design based on (a), while further optimization is illustrated in design (c). Every add-on stage will encroach on certain area of either the absorber or the thermal isolation structure, resulting in the absorbers of the stages higher than the triple-stage too small to collect enough infrared radiation.

On the first optimization step, the proper area of the absorber has been investigated to maximize the efficiency of space utilization with the consideration of the integrated metalens. The metalens at the back of the FPA chip converges the incoming radiation, leading to the nonlinear increasement of absorptance with the absorber area. In our previous work, we found that the increasing rate undergoes a substantial drop when the size of the absorber goes beyond 26 $\mu$m × 26 $\mu$m, where roughly 86% of incident radiation can be absorbed [28]. Therefore, the absorber is downsized to 26 $\mu$m × 26 $\mu$m from the initial size of 26 $\mu$m × 58 $\mu$m, while keeping the absorption almost intact. The shrinkage of the absorber frees up some space in the middle of the pixel, which, however, is hard to be filled by long-straight structures arranged on the outside. Considering it's the length of the isolation beams that matters rather than the shape, multiple folded isolation beams are arranged inside to fill in the space freed up by the absorber. As a result, the conductive thermal resistance increased significantly in 1b & 2b designs compared with the initial 1a & 2a designs. On the second optimization step, the arrangement of isolation beams has been studied further. Despite two long isolation beams, the thermal resistance is limited because of the parallel connection. Hence, using single long isolation beam can greatly improve the thermal

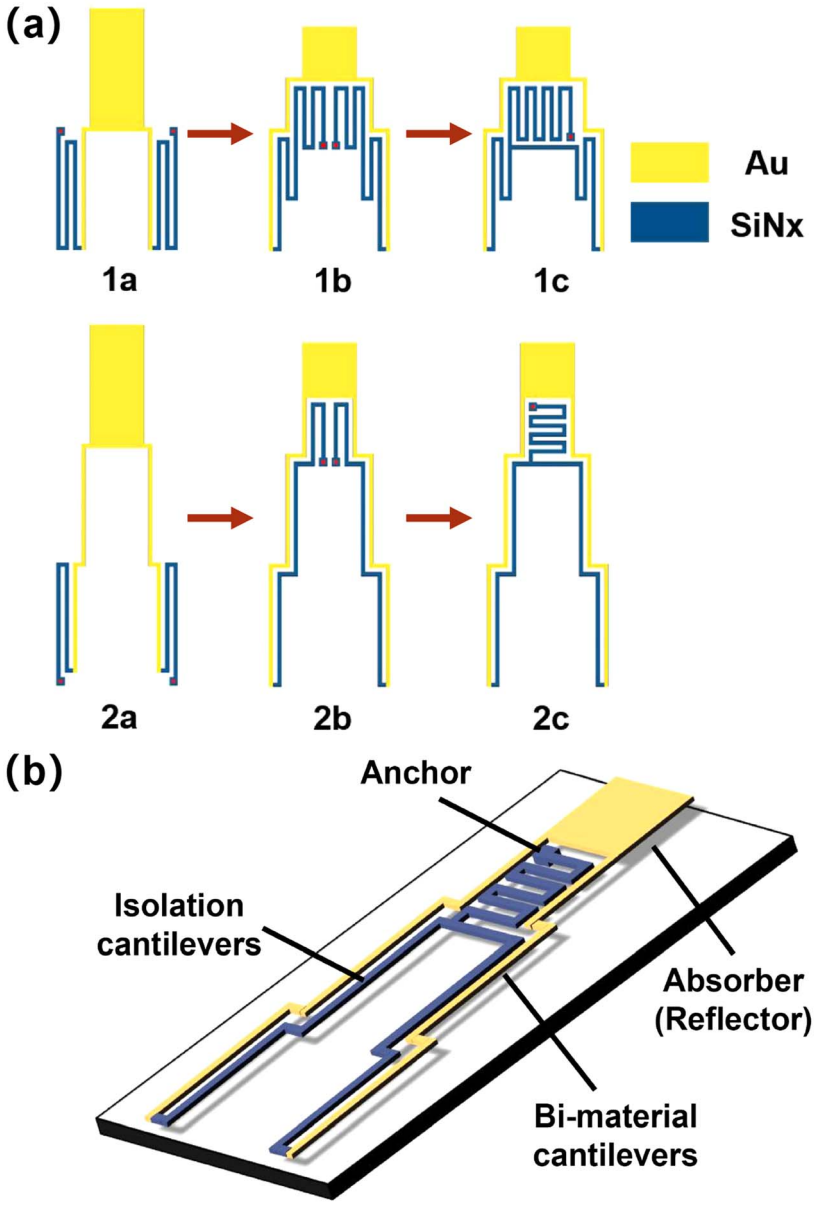


**Figure 3.** (a) layout of designed pixel structures. (b) Detailed structure diagram of structure 2c.

resistance. However, the loss of the symmetry could destabilize the structure, which is not appreciated for the subsequent optical readout. Thus, a series-parallel connection strategy was adopted, in which only the latter part of the two thermal isolation beams have be combined into one with the anchor near the central axis of the structure. Therefore, greater thermal resistance and higher thermal conversion efficiency can be obtained while ensuring adequate balance of the structure.

## 3. Performance analysis

### 3.1. Thermal response $H^*S_T$

The geometric parameters of the pixel structures are listed in table 2.

$A_{ab}$ in equation (2) is the absorption area in a conventional pixel structure without integrated metalens. In the uniform irradiation case, the infrared radiation received by the absorber varies linearly with its area. However, with a metalens, the infrared radiation absorption is no longer proportional to the size of the absorber area, thus the equivalent area $A_e$ is used as a substitute for the calculation of thermal conversion efficiency, which can be denoted by:

$$A_e = \eta \cdot A_{pixel} \tag{8}$$

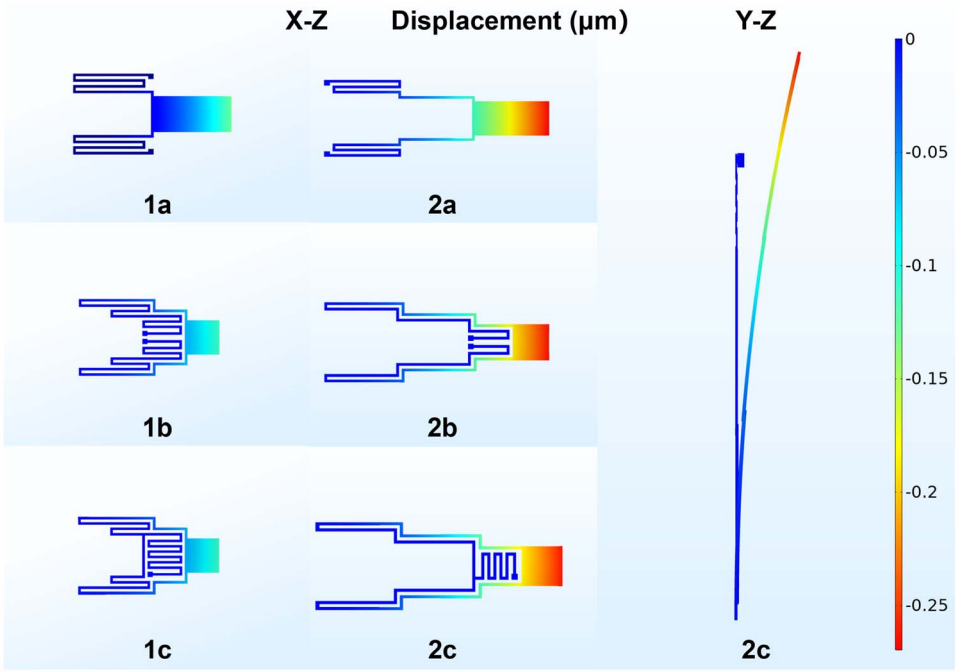


**Figure 4.** Thermal deflection simulations on X–Z plane and Y–Z plane ($\Delta T = 1K$).

**Table 2.** Parameters of the designed pixel structures.[a]

| | Absorber size A $\mu$m×B $\mu$m | Length of thermomechanical cantilevers $L_m$ $\mu$m | Length of isolation beams $L_{leg}$ $\mu$m | Width of cantilevers $t$ $\mu$m |
|---|---|---|---|---|
| 1a | 26 × 58 | 114 | 164//164 | 2 |
| 1b | 26 × 26 | 106 | 236//236 | 2 |
| 1c | 26 × 26 | 106 | (115//147)&223 | 2 |
| 2a | 26 × 58 | 164 | 110//110 | 2 |
| 2b | 26 × 26 | 162 | 180//180 | 2 |
| 2c | 26 × 26 | 162 | (123//139)&119 | 2 |

[a] '//' indicates a parallel relationship, while '&' concatenation.

where $\eta$ represents the effective fill factor and is defined as the ratio of the energy in the photosensitive area to the total energy incident in the entire aperture, which is the predetermined pixel size $A_{pixel} = 3600\mu m^2$. There are two sizes of absorber in the designed structures, 26 $\mu$m × 58 $\mu$m and 26 $\mu$m × 26 $\mu$m. Converged by metalens, the effective fill factor for the absorber with an area of 26 $\mu$m × 58 $\mu$m is $\eta_1 = 93\%$, while $\eta_2 = 86.5\%$ for the absorber with an area of 26 $\mu$m ×26 $\mu$m. Following equations (2)–(4) & (8), thermal conversion efficiencies can be calculated.

Thermal mechanical sensitivity $S_T$ can be evaluated with equations (5) & (6) by approximating the pixel as a single straight beam. Considering the wiggle structure of the bi-material section of the designs in figure 3, numerical simulations have been carried out using COMSOL to obtain a more precise evaluation and the results are shown in figure 4.

The thermal and thermomechanical properties of each design are listed in table 3. Comparing the design a and design b, owing to the convergence of the incident energy with metalens, the absorption experienced a reduction less than 7% even though the absorber area was reduced by more than 55%. It means that much space can be saved for the thermal isolation structures with a slight reduction in absorption. Therefore, from design a to design b, the thermal conductance of the thermal isolation legs $G_{leg}$ experienced a 32% (39%) drop resulting in a higher $H$, while the thermomechanical sensitivity decreased by only 12% (3%). Moreover, further improvement of thermal isolation was achieved with design c with a more than 50% of reduction in $G_{leg}$. As a result, thermal conversion efficiency $H$ of design (c) increased by 75% (60%) compared with design (b). Therefore, the overall thermal response of double-stage and triple-stage nested design (c) improved by 85% and 123% compared with initial design (a), respectively.

**Table 3.** Basis performance of the designed structures.

| | 1a | 1b | 1c | 2a | 2b | 2c |
|---|---|---|---|---|---|---|
| $G_{leg} \times 10^{-9}$ W/K | 68.75 | 46.61 | 19.13 | 100 | 61.11 | 29.85 |
| $G_{rad} \times 10^{-9}$ W/K | 17.86 | 17.86 | 17.86 | 17.86 | 17.86 | 17.86 |
| $G_{total} \times 10^{-9}$ W/K | 86.61 | 64.47 | 36.99 | 117.86 | 78.97 | 47.71 |
| $H$ | 0.010 | 0.012 | 0.021 | 0.007 | 0.010 | 0.016 |
| $S_T$ $\mu$m/K | 0.130 | 0.114 | 0.113 | 0.273 | 0.266 | 0.264 |
| $H^*S_T \times 10^{-3}$ $\mu$m/K | 1.30 | 1.39 | 2.42 | 1.95 | 2.66 | 4.34 |

### 3.2. Noise-equivalent temperature difference

Noise-equivalent temperature difference (NETD) is the minimum temperature change in an IR source that can be detected with a signal-to-noise ratio of unity, defining the performance of an IR imaging system. The NETD of the system is determined by three parts of noise: inherent noise limited by the FPA itself, noise introduced by the readout system and base temperature fluctuation. Inherent NETD limited by the FPA is typically referred to as the detection limit, while other noises can be significantly reduced by better experimental conditions or utilizing a thermal stabilizing system [31]. Thus, only the inherent noise of FPA, which arises from temperature fluctuation and thermomechanical vibration, is taken into consideration.

#### *3.2.1. Thermodynamic fluctuation noise*

Based on the statistical nature of the heat exchange with the environment, thermodynamic fluctuation noise occurs in any thermodynamic system exhibiting random fluctuations in temperature. For the cantilever pixel, the mean square temperature fluctuation at low-frequency range is:

$$\Delta T_{th} = \sqrt{\frac{4k_B T^2 B}{G_{total}}}; G_{total} = G_{rad} + G_{leg} \tag{9}$$

where $G_{total}$ is the total thermal conductance from the cantilever to environment, $k_B$ Boltzmann's constant, $T$ the cantilever's temperature (~300 K), and $B$ the detection bandwidth (=30 Hz).

#### *3.2.2. Vibration noise*

Vibration noise arises from two sources: thermal and external. Thermomechanical vibration in a mechanical system comes from thermal energy and is fundamental in nature while the external vibration can be experimentally alleviated and thus not discussed. The noise at off-resonant frequencies can be calculated as:

$$\delta_{th,vib} = \sqrt{\frac{4k_B T \Delta f}{g\omega_0 Q}} \tag{10}$$

where $\Delta f$ is the measurement bandwidth, which is typically about 30 Hz for a CCD detector; $Q$ the resonance quality factor, which is the ratio of the vibration amplitude at resonant frequency to that at off-resonant frequency; and $Q$ is typically about 10 at atmospheric pressure, and 100–1000 in vacuum ($Q = 500$ for our calculation). $g$ and $\omega_0$ are the cantilever's spring constant and the system resonant frequency respectively, which can be obtained by simulating [14]. Using the thermomechanical sensitivity of the cantilever, thermomechanical noise can be converted to an equivalent temperature fluctuation as:

$$\Delta T_{th,vib} = \frac{\delta_{th,vib}}{S_T} \tag{11}$$

Thus, NETD can be obtained as:

$$\Delta T_{FPA} = \sqrt{\Delta T_{th}{}^2 + \Delta T_{th,vib}{}^2}, \ \mathrm{NETD}_{FPA} = \frac{\Delta T_{FPA}}{H} \tag{12}$$

### 3.3. Thermal response time $\tau$

The thermal response time $\tau$ is determined by $C_{th}$ and $G_{total}$, the total heat capacity of the bi-material part of the cantilever and the thermal conductance between the cantilever and environment, which can be expressed as:

$$\tau = \frac{C_{th}}{G_{total}}; C_{th} = \sum(\rho V c)_i \tag{13}$$

in which $\rho$ is the material density, $V$ the volume, $c$ the material heat capacity and $i$ indicates each material used in the cantilever element. Equation (13) indicates that better thermal isolation will result in a slowdown in the time response of the pixel.

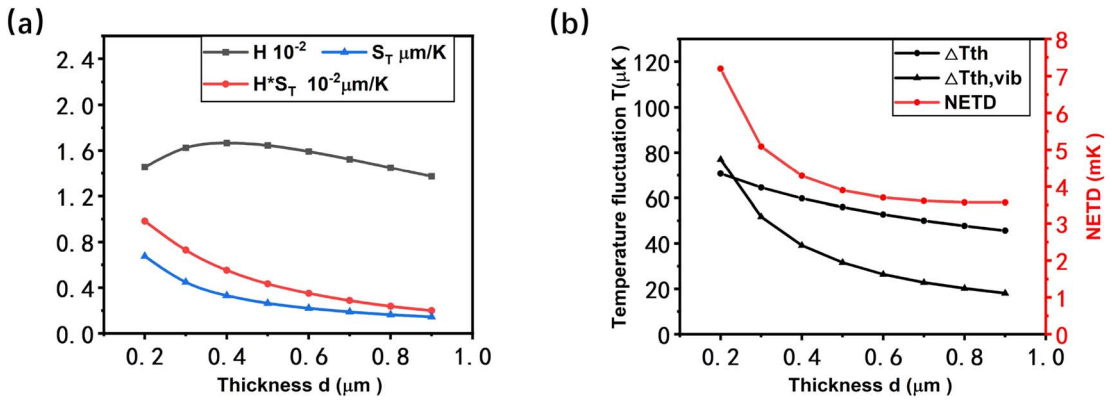


**Figure 5.** Variations of performances with the thickness of Si $N_x$ in condition of $d_{Au} = 0.7d_{SiN_x}$. (a) Thermomechanical sensitivity $S_T$, thermal conversion efficiency $H$ and thermal response $H^* S_T$. (b) The mean square temperature fluctuation $\Delta T_{th}$, $\Delta T_{th,vib}$ and $NETD_{FPA}$.

**Table 4.** NETD and response time $\tau$ of the designed structures.

| | 1a | 1b | 1c | 2a | 2b | 2c |
|---|---|---|---|---|---|---|
| $g \times 10^{-3} N/m$ | 5.34 | 7.76 | 4.96 | 2.97 | 3.72 | 3.40 |
| $\omega_0 Hz$ | 4737 | 4737 | 5668 | 3075 | 4401 | 4229 |
| $\Delta T_{th}$ $\mu$K | 41.48 | 48.08 | 63.48 | 35.56 | 43.44 | 55.89 |
| $\Delta T_{th,vib}$ $\mu$K | 48.2 | 45.6 | 52.6 | 38.2 | 29.3 | 31.5 |
| $NETD_{FPA}$ mK | 6.36 | 5.46 | 3.85 | 7.31 | 5.24 | 3.90 |
| $\tau$ *ms* | 38.56 | 29.02 | 50.57 | 31.22 | 28.51 | 47.19 |
| FOM *mK* • *ms* | 245.4 | 158.4 | 194.6 | 228.3 | 149.3 | 184.2 |

### 3.4. Figure of merit

Figure of Merit(FOM) is used to recognize the tradeoff between thermal time constant and sensitivity [32], which can be written as:

$$\text{FOM} = \text{NETD} \bullet \tau \tag{14}$$

And a smaller FOM is better.

Table 4 lists the predicted performance including NETDs, response times $\tau$, and FOM of the designed structures. The optimizations effectively reduce NETDs by almost half, but with the sacrifices of the response times. With higher thermal response, lower NETD and over 20 frames per second, design (c) is able to work well for higher sensitivity in low framerate scenarios. However, in cases that need to take both NETD and response time into consideration, design (b) with lower FOM can be a better choice. In addition, reliability and stability is also important for a device. It can be seen that the reduction of anchors from design (b) to design (c) only slightly reduces the spring constant $g$ of the FPA structure and does not have a substantial impact on the system resonant frequency $\omega_0$, and therefore has a limited effect on the reliability and stability of the device.

### 3.5. The thickness effects of $SiN_x$ film

The thickness of $SiN_x$ film has direct effects on both thermal conversion efficiency $H$ and thermomechanical sensitivity $S_T$. The thickness of $SiN_x$ film $d_2$ defines the absorption length of the incoming IR radiance. It should be emphasized that IR radiation travels twice as far in $SiN_x$ as its thickness because Au is extremely reflective of infrared radiation. Hence, the absorption length $l_p$ in equation (3) is equal to $2d_2$. Although thicker film could ensure more absorption on incoming energy, the thermal isolation would get worse due to larger cross section of the beam ($A_{Leg}$ in equation (4)). On the other hand, thermomechanical sensitivity $S_T$ is inversely proportional to $d_2$ according to equation (5). Therefore, as a combined effect, thermal response $H^* S_T$ increases as the film get thinner. However, the noise analysis indicates that thinner beam would provoke larger vibration noise $\delta_{th,vib}$ since the spring constant of the cantilever $g$ is proportional to the cubic of the beam thickness $d_2$. As a result, even though with thinner beam, the cantilever is more sensitive to IR radiation, the sensor is subject to the vibration noise, leading to the deterioration of the overall performance (NETD). The variations of thermal response and NETD along with film thickness $d_2$ are illustrated in figure 5. It can be observed that at the range of

$0.2 \sim 0.9\mu$m, the thicker the beam, the lower the NETD. But it is not difficult to see that as $d_2$ exceeds 0.5 $\mu$m, further increase in $d_2$ would induce negligible gain in NETD. Hence, with the consideration of fabrication cost, etc, the optimized thickness of $SiN_x$ film is set to be 0.5 $\mu$m.

## 4. Conclusion

The sensitivity of an optomechanical FPA relies on long thermal isolation structure, long thermomechanical cantilever, and also large fill factor, which are usually hard to achieve simultaneously. By integrating a designed metalens, the spatial competition among the key elements of the FPA can be alleviated without complicating manufacturing. In this study, based on the initial nested structure, various optimized designs of optomechanical FPAs with integrated metalens array are analyzed and evaluated. The convergence of incident IR signal by the pixelated metalenses enables high effective fill factors with a small IR absorption area. The reduction of the IR absorption area frees up the space for longer thermal isolation beams and also the thermal deformation cantilevers. Therefore, both the thermal conversion efficiency and thermomechanical sensitivity experience significant improvements simultaneously. Compared with the initial double anchor designs, the single anchor arrangements (1c and 2c) further reduce the heat loss on the sensors. The theoretical and simulation results indicate that the single-anchor, triple-stage design achieves high thermal conversion efficiency $H = 0.016$ and thermomechanical sensitivity $S_T = 0.264\mu$m/K. Hence, the combination performance $H^* S_T$ increases by more than 3 folds compared with the initial design (1a). With the consideration of thermodynamic fluctuation noise and thermal vibration noise, an inherent NETD value of 3.9mK at the preset $60\mu$m $\times$ $60\mu$m pixels is achieved. However, as NETD decreases, the response time correspondingly increases. Based on the consideration of FOM and application, design (c) is able to work well for higher sensitivity in low framerate scenarios and design (b) is a better choice for scenarios where NETD and response time are both important. Furthermore, the influence of thickness of bi-material cantilevers is further discussed on the performance of FPA. Notably, partial absorption of the radiated energy within the $SiN_x$ film is discussed even though the thickness of absorbing material exceeds the penetration depth. Consequently, the absorption of incident infrared radiation determined by the thickness of absorbing material is introduced into the calculation of thermal conversion efficiency as a factor to ensure a more precise optimization. And it is found that $d_{SiN_x} = 0.5$ $\mu$m can be the best choice.

## Acknowledgments

This work was financed by the National Natural Science Foundation of China (#12172348 & #12302251). We would like to thank the USTC Center for Micro and Nanoscale Research and Fabrication and Experimental Center of Engineering and Material Sciences of USTC.

## Data availability statement

All data that support the findings of this study are included within the article (and any supplementary files).

## ORCID iDs

Yang Zhao https://orcid.org/0000-0002-3962-2793

## References

[1] Švantner M *et al* 2022 Statistical study on human temperature measurement by infrared thermography *Sensors* **22** 8395
[2] Ring E F J 2007 The historical development of temperature measurement in medicine *Infrared Phys. Technol.* **49** 297–301
[3] Soref R 2010 Mid-infrared photonics in silicon and germanium *Nat. Photonics* **4** 495–7
[4] Diakides M, Bronzino J D and Peterson D R 2012 *Medical Infrared Imaging: Principles and Practices* (CRC press)
[5] Leonidas E *et al* 2022 A comparative review of thermocouple and infrared radiation temperature measurement methods during the machining of metals *Sensors* **22** 4693
[6] Castro P *et al* 2020 Infrared temperature measurement sensors of overhead power conductors *Sensors* **20** 7126
[7] Ourinson D *et al* 2020 In situ surface temperature measurement in a conveyor belt furnace via inline infrared thermography *J. Vis. Exp.* **159** e60963
[8] Antoni R J I 2002 Infrared detectors: an overview *Infrared Phys. Technol.* **43** 187–210
[9] Vollmer M and MöLlmann K P 2017 Infrared thermal imaging (fundamentals, research and applications) *Microsystems* 615–44
[10] Rogalski A 2000 *Infrared Detectors* (CRC press)
[11] Ramaiah M R *et al* 2020 Wavelength dependence of photothermal deflection in Au/Si bimaterial microcantilevers *Sens. Actuators, A* **315** 112233
[12] Zhu H *et al* 2022 A terahertz optomechanical detector based on metasurface and Bi-material micro-cantilevers *Micromachines* **13** 805

[13] Lai J et al 1997 Optimization and performance of high-resolution micro-optomechanical thermal sensors *Sensors and Actuators A: Physical* **58** 113–9
[14] Ma W et al 2016 Bimaterial cantilever focal plane array for uncooled infrared imaging using sandwich-framed structure *J. Microelectromech. Syst.* **25** 413–20
[15] Yang A et al 2016 Nanoantenna integrated thermomechanical infrared detector *Plasmonics* **12** 1921–7
[16] Zhang P et al 2020 Highly aligned carbon nanotube-based bi-material microactuators with reduced intertube slipping *ChemNanoMat* **6** 404–11
[17] Dong F et al 2007 An uncooled optically readable infrared imaging detector *Sensors and Actuators A: Physical* **133** 236–42
[18] Teng C et al 2009 Analysis of optical readout sensitivity for uncooled infrared detector *Chinese Physics Letters* **26** 124206
[19] Zhao Y et al 2002 Optomechanical uncooled infrared imaging system: Design, microfabrication, and performance *J. Microelectromech. Syst.* **11** 136–46
[20] Dong F et al 2007 An uncooled optically readable infrared imaging detector *Sens. Actuators, A* **133** 236–42
[21] Dong F et al 2008 Uncooled infrared imaging device based on optimized optomechanical micro-cantilever array *Ultramicroscopy* **108** 579–88
[22] Cheng T et al 2009 Performance of an optimized substrate-free focal plane array for optical readout uncooled infrared detector *J. Appl. Phys.* **105** 034505
[23] Toy M F et al 2009 Uncooled infrared thermo-mechanical detector array: Design, fabrication and testing *Sens. Actuators, A* **156** 88–94
[24] Shang Y et al 2015 Design, fabrication, and characterization of a polymer-based MEMS Uncooled infrared focal plane array *J. Microelectromech. Syst.* **24** 1132–41
[25] Li F et al 2020 HgCdTe mid-Infrared photo response enhanced by monolithically integrated meta-lenses *Sci. Rep.* **10** 6372
[26] Zhang P 2021 *Research on Photomechanical Uncooled Infrared Focal Plane Based on Super-aligned Carbon Nanotubes* (University of Science and Technology of China)
[27] Cetin R et al 2018 Design, analysis and implementation of quarter-wave absorber structure for uncooled infrared detectors with high fill factor *43rd International Conference on Infrared, Millimeter, and Terahertz Waves (IRMMW-THz)* 1–2
[28] Hou H et al 2022 Design and fabrication of monolithically integrated metalens for higher effective fill factor in long-wave infrared detectors *Opt. Lasers Eng.* **150** 106849
[29] Cheng T et al 2009 Optical readout sensitivity of deformed microreflector for uncooled infrared detector: theoretical model and experimental validation **26** 2353–61
[30] Zhao Y 2002 *Optomachanical Uncooled Infrared Imaging System* (University of California, Berkeley)
[31] Choi J et al 2003 Design and control of a thermal stabilizing system for a MEMS optomechanical uncooled infrared imaging camera *Sens. Actuators, A* **104** 132–42
[32] Kohin M and Butler N R 2004 *Performance limits of uncooled VOx microbolometer focal plane arrays. in Infrared Technology and Applications XXX* (SPIE)